RESEARCH ARTICLE

Effects of Mg Component Ratio on Photodetection Performance of MgGa$_2$O$_4$ Solar-Blind Ultraviolet Photodetectors

Qichao Hou, Kewei Liu,* Xing Chen,* Jialin Yang, Qiu Ai, Zhen Cheng, Yongxue Zhu, Binghui Li, Lei Liu, and Dezhen Shen*

Mg$_x$Ga$_2$O$_4$ epitaxial films with different Mg component ratios ($x = 0.6$, 0.8, 1, 1.1, and 1.4) and their metal–semiconductor–metal solar-blind ultraviolet (SBUV) photodetectors are prepared on *c*-face sapphire by metal–organic chemical vapor deposition (MOCVD). The structure, composition, crystalline quality, and optical properties of the Mg$_x$Ga$_2$O$_4$ thin films have been investigated in detail. It can be found that five Mg$_x$Ga$_2$O$_4$ thin films have the spinel structure with a similar bandgap of ≈ 5.15 eV, and the highest crystalline quality is observed in Mg$_x$Ga$_2$O$_4$ with $x = 1$. Besides, photodetector based on Mg$_x$Ga$_2$O$_4$ film with $x = 1$ has the highest responsivity, the largest UV–visible rejection ratio, and the fastest response speed. As the content of Mg deviates from the stoichiometric ratio of MgGa$_2$O$_4$, the crystalline quality of the Mg$_x$Ga$_2$O$_4$ thin film is reduced, and their photoelectric response characteristics are deteriorated. This work indicates that MgGa$_2$O$_4$ is a promising candidate for the applications in high-performance solar-blind ultraviolet photodetectors.

1. Introduction

Solar-blind ultraviolet (SBUV) photodetectors have broad application prospects in military and civil fields such as missile warning, space security communications, environmental monitoring, and fire monitoring due to their low background noise, high sensitivity, and strong anti-jamming ability.[1–3] In recent years, owing to the unique advantages of all-solid state, small size, intrinsic solar blindness, high thermal and chemical stability, strong radiation resistance, and low energy consumption, SBUV photodetectors

Q. Hou, K. Liu, X. Chen, J. Yang, Q. Ai, Z. Cheng, Y. Zhu, B. Li, L. Liu, D. Shen
State Key Laboratory of Luminescence and Applications
Changchun Institute of Optics, Fine Mechanics and Physics, Chinese Academy of Sciences
Changchun 130033, P. R. China
E-mail: liukw@ciomp.ac.cn; chenxing@ciomp.ac.cn; shendz@ciomp.ac.cn

Q. Hou, K. Liu, X. Chen, J. Yang, Q. Ai, Z. Cheng, Y. Zhu, B. Li, L. Liu, D. Shen
Center of Materials Science and Optoelectronics Engineering
University of Chinese Academy of Sciences
Beijing 100049, P. R. China

The ORCID identification number(s) for the author(s) of this article can be found under https://doi.org/10.1002/pssr.202200137.

fabricated from wide-bandgap semiconductors including AlGaN,[4–7] Ga$_2$O$_3$[8–13] and ZnMgO,[14–16] have attracted significant attention and are generally considered to be the next generation of UV photodetectors. However, the preparation of high-quality AlGaN with high Al composition suitable for solar-blind detection still faces many challenges due to the significant lattice and thermal mismatches between the AlGaN layer and the hetero-substrate and the high surface migration barrier of Al atoms. As for ZnMgO ternary alloy with a certain Mg content, the different crystal structures of ZnO (wurtzite) and MgO (rock salt) often lead to phase separation.[5,16] As a binary compound, the optical, electrical, and optoelectronic properties of Ga$_2$O$_3$ are difficult to tune on a large scale without doping with other elements. More recently, ternary complex oxide wide bandgap semiconductors represented by ZnGe$_2$O$_4$,[17–19] ZnGa$_2$O$_4$,[20–24] MgGa$_2$O$_4$,[25] etc. have been extensively studied for SBUV photodetectors thanks to their suitable bandgap, easily tuned physical properties by adjusting the components, high stability, and so on. Among them, spinel-structured MgGa$_2$O$_4$, with an ultra-wide bandgap of ≈ 4.9 eV,[26,27] has been used successfully as phosphors for a long time. Surprisingly, we recently discovered in 2022 that solar-blind UV detectors based on O$_2$-annealed MgGa$_2$O$_4$ epitaxial films exhibit ultrafast response speed and a high UV-visible rejection ratio.[25] In addition, MgGa$_2$O$_4$ also offers the added benefits of flexible structure and properties of spinel oxide with two metal cations. Therefore, it is expected that MgGa$_2$O$_4$ has great potential in the field of high-performance SBUV photodetection.

For AB$_2$O$_4$ spinel structure, oxygen ions are cubic close-packed, and cations occupy 1/8 of the tetrahedral sites and 1/4 of the octahedral sites. According to the previous studies,[28] MgGa$_2$O$_4$ has a partially inverse spinel structure with an inversion index of between 0.81 and 0.87 at room temperature, indicating the disordered distribution of its metal cations. As a result, the optical, electrical, and optoelectronic properties of MgGa$_2$O$_4$ vary significantly with the components of Mg and Ga cations.[29–34] Therefore, studying the effect of the cation ratio on the characteristics of MgGa$_2$O$_4$ is helpful to realize high-performance SBUV photodetectors, but no related research has yet been reported.

In this study, Mg$_x$Ga$_2$O$_4$ epitaxial films with different Mg component ratios ($x = 0.6$, 0.8, 1, 1.1, and 1.4) and their

metal–semiconductor–metal (MSM) photodetectors were prepared on c-Al_2O_3 (0001) substrates by metal–organic chemical vapor deposition (MOCVD) by regulating the carrier gas flow rate of Mg source. The effects of Mg composition on the crystal structure, surface morphology, optical and photoelectric properties of SBUV photodetectors based on $Mg_xGa_2O_4$ thin films were studied. Although the content of Mg deviates from the stoichiometric ratio, the results of X-ray diffraction (XRD) show that all samples maintain the spinel structure of $MgGa_2O_4$. Moreover, among the $Mg_xGa_2O_4$ SBUV photodetectors with different Mg compositions, the device with $x = 1$ has the highest responsivity and the fastest response speed. As the content of Mg deviates from the stoichiometric ratio, the photodetection performance of the devices tends to decrease. The mechanism of this phenomenon is analyzed in detail. Our work lays a foundation for further improving the performance of $MgGa_2O_4$ SBUV photodetectors.

2. Results and Discussion

The compositions of $Mg_xGa_2O_4$ films with different Mg source flow rates were estimated by X-ray energy dispersive spectroscopy (EDS). **Figure 1**a is a typical EDS spectrum of $Mg_xGa_2O_4$ film fabricated with an Mg source flow rate of 10 sccm. It can be seen that the main elements of this sample are O, Ga, Mg, and Al (the signal of Al comes from the sapphire substrate), and Mg component ratio x can be calculated to be ≈ 1 in this case ($MgGa_2O_4$) using the equation of $x = 2*(Mg\ At\%)/(Ga\ At\%)$. Figure 1b presents the Mg component ratio x as a function of the Mg source flow rate. Clearly, the Mg composition of $Mg_xGa_2O_4$ film estimated from the EDS result increases with increasing the Mg source flow rate. When the Mg source flow rate was 5, 7.5, 10, 12.5, and 15 sccm, the Mg composition x of $Mg_xGa_2O_4$ films were 0.6, 0.8, 1, 1.1, and 1.4, respectively.

To characterize the crystal structure of the materials, the XRD measurements were carried out on $Mg_xGa_2O_4$ films. **Figure 2**a shows the XRD θ-2θ scan spectra. The sharp peaks at $2\theta = 20.8°$ and $41.68°$ can be indexed to (0003) and (0006) Bragg peaks of the sapphire substrate, respectively. Besides that, all samples have three diffraction peaks at about $2\theta = 18.6°$, $37.8°$, and $58°$, which correspond exactly to the (111), (222), and (333) diffraction planes

of the spinel $MgGa_2O_4$ (JCPDS No. 73-1721), respectively. Notably, with the increase of Mg content in the film, the diffraction peak position of (222) gradually shifts toward a lower 2θ angle, which may be associated with the substitution of smaller Ga^{3+} ions by bigger Mg^{2+} ions. Enlarged XRD patterns near (222) peaks (2θ range from 35° to 40°) are shown in Figure S1, Supporting Information, and the movement of the (222) peak can be clearly seen from this figure. The XRD θ-2θ scan results indicate that all $Mg_xGa_2O_4$ thin films have spinel structure preferentially grown along the [111] direction without any other crystal phases. Figure 2b presents the rocking curves of the diffraction peak from the (222) plane. The narrowest full width at half maximum (FWHM) of only 0.0615° is observed for the $Mg_xGa_2O_4$ film with $x = 1$, indicating its highest crystalline quality. As the content of Mg deviates from the stoichiometric ratio of $MgGa_2O_4$ spinel, the FWHM tends to increase, implying the degradation of the crystalline quality of $Mg_xGa_2O_4$ films. The optical transmission spectra of the $Mg_xGa_2O_4$ films with different Mg contents are shown in Figure 2c. All the samples exhibit an average transmittance of over 90% in the wavelength range from 300 to 700 nm. In addition, a sharp absorption edge can be observed at ≈ 240 nm for all samples. With increasing Mg content from 0.6 to 1.4, the bandgaps of the corresponding films do not change significantly, which are about 5.15 eV as shown in Figure 2d.

The surface morphology and film thickness of $Mg_xGa_2O_4$ films were measured by scanning electron microscope (SEM) as shown in **Figure 3**. It can be seen that the thickness of $Mg_xGa_2O_4$ films is between 190 and 225 nm. In addition, the atomic force microscopy (AFM) results indicate that all the $Mg_xGa_2O_4$ films have a relatively flat surface with root mean square (rms) roughness of 5–6 nm (see Figure S2, Supporting Information).

To further study the effect of Mg content on the SBUV photodetection performance of $Mg_xGa_2O_4$ thin films, the MSM SBUV photodetectors with 25 pairs of gold interdigitated electrodes (≈ 50 nm thick) were fabricated on these films by conventional photolithography and lift-off process. The schematic device structure is shown in **Figure 4**a. The finger width and spacing of the interdigital electrodes are both 10 μm, and the interdigital length is 500 μm.
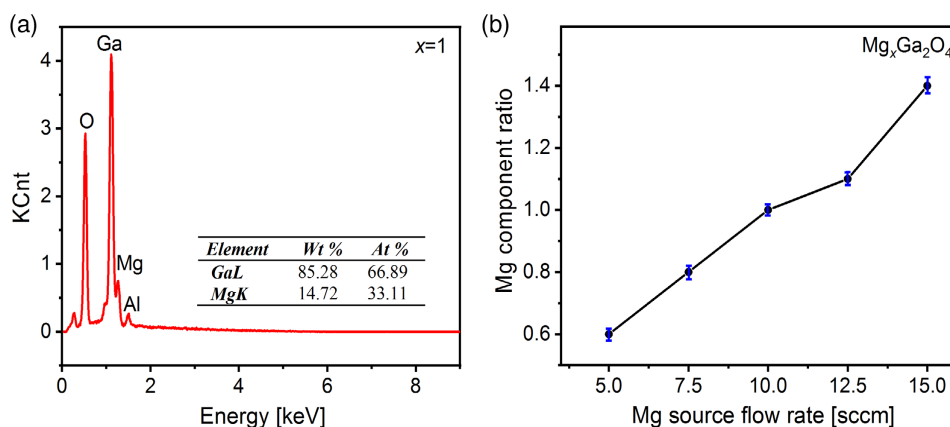

Figure 1. a) Typical energy dispersive spectroscopy (EDS) spectrum of $Mg_xGa_2O_4$ film with $x = 1$ and b) Mg component ratio x of $Mg_xGa_2O_4$ films as a function of Mg source flow rate with error bars.
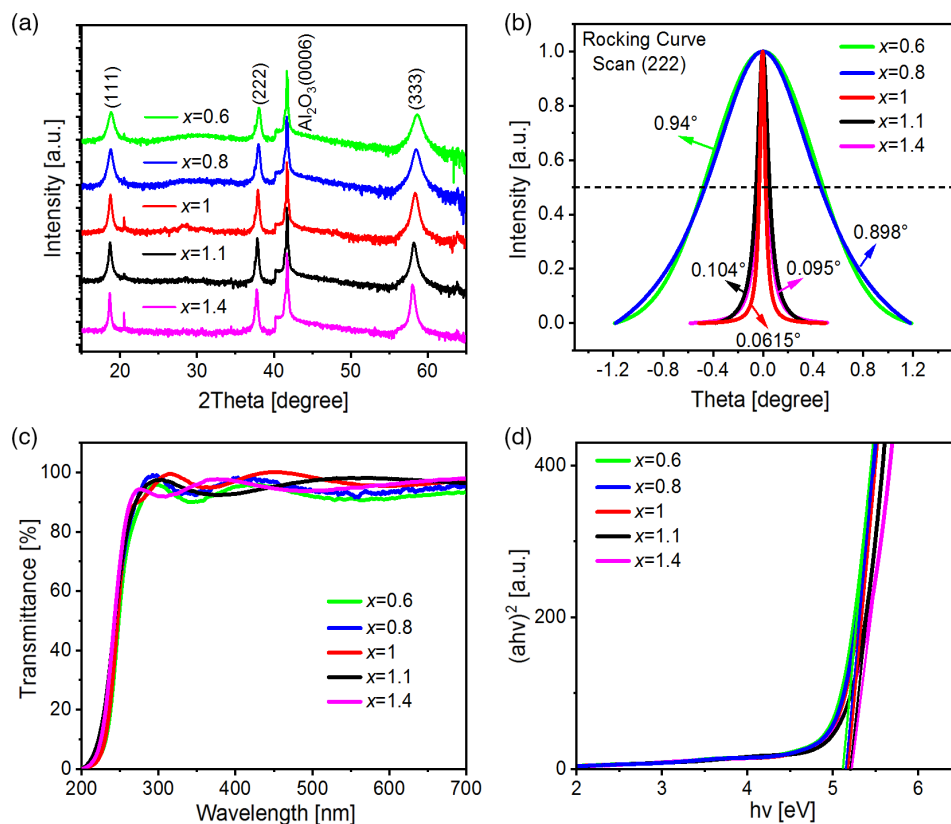
Element	Wt %	At %
GaL	85.28	66.89
MgK	14.72	33.11

pss rrl
physica status solidi
www.pss-rapid.com

Figure 2. X-ray diffraction (XRD) a) θ-2θ scan and b) normalized rocking curves for the (222) plane of $Mg_xGa_2O_4$ films with different Mg contents. c) Transmission spectra of $Mg_xGa_2O_4$ thin films and d) a plot of $(\alpha h\nu)^2$ as a function of photon energy ($h\nu$).

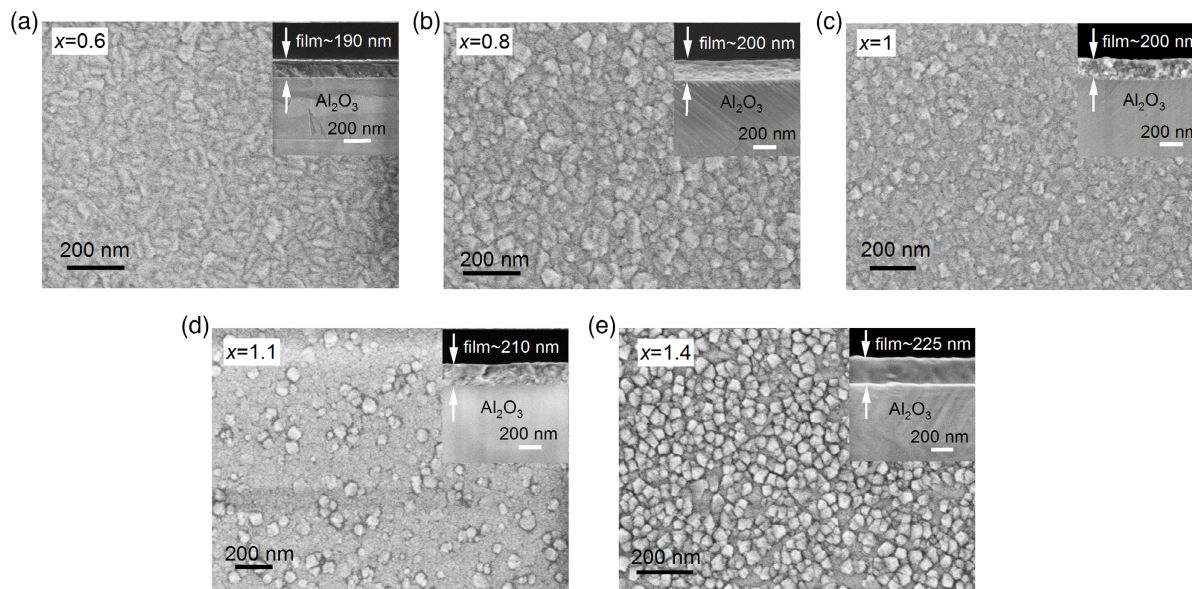**Figure 3.** a–e) Top and cross-sectional SEM images patterns of $Mg_xGa_2O_4$ thin films with different Mg contents.

The current–voltage (I–V) characteristic curves of $Mg_xGa_2O_4$ SBUV photodetectors were measured both in the dark and under 254 nm UV light illumination by a semiconductor parameter analyzer. As shown in Figure 4b, the dark current of all five devices is less than 15 pA at 10 V bias. For Mg-poor $Mg_xGa_2O_4$ ($x = 0.6$ and 0.8) devices, the replacement of Mg sites

ADVANCED
SCIENCE NEWS
www.advancedsciencenews.com

pss rrl
physica status solidi
www.pss-rapid.com

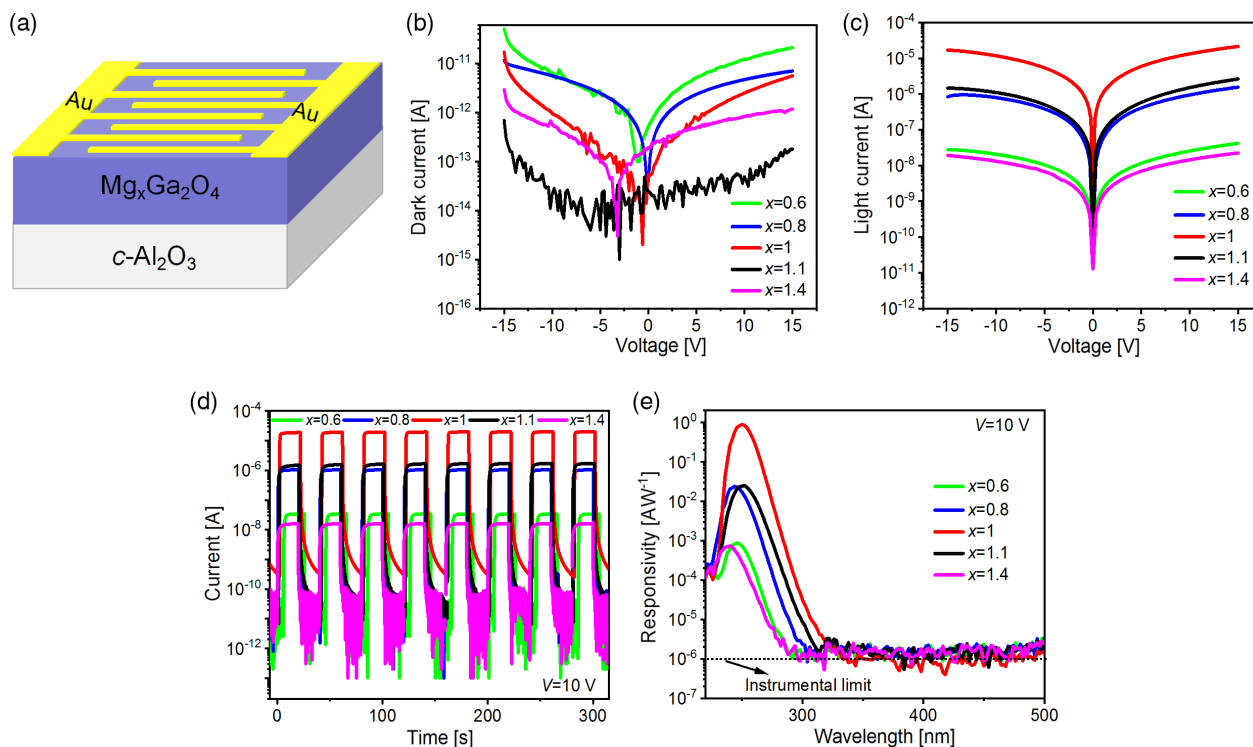**Figure 4.** a) Schematic illustration of the solar-blind ultraviolet (SBUV) metal–semiconductor–metal (MSM) photodetectors based on $Mg_xGa_2O_4$ films. b) I–V curves under dark conditions. c) I–V curves under 254 nm UV light illumination. d) I–t curves of $Mg_xGa_2O_4$ SBUV photodetectors and e) spectral response of SBUV photodetectors under 10 V bias with y-axis in logarithmic scale.

with Ga atoms or Mg vacancy can act as donors, resulting in the increase of the dark current. In contrast, the replacement of Ga sites with Mg atoms in Mg-rich $Mg_xGa_2O_4$ ($x = 1.1$ and 1.4) can act as acceptors, which can compensate for the small amount of donors associated with oxygen vacancies, thereby reducing the dark current of the device. Notably, the device based on $Mg_{1.1}Ga_2O_4$ thin film exhibits the lowest dark current (22 fA). Under a bias of 10 V, the device based on the film with $x = 1$ showed the biggest light current among the five devices due to the highest crystalline quality, as shown in Figure 4c. The I–t characteristic of the photodetectors was measured by periodically turning on and off the 254 nm UV light illumination ($\approx500\,\mu W\,cm^{-2}$) under 10 V bias as shown in Figure 4d. All five devices exhibit high stability and repeatability photocurrent responses with a fast response speed. Moreover, the light-to-dark current ratio (I_{light}/I_{dark}) can reach as high as 1×10^5 for the device based on $Mg_xGa_2O_4$ thin film with $x = 1$.

Figure 4d represents the spectral response characteristic curves of $Mg_xGa_2O_4$ SBUV photodetectors. It can be found that all devices have obvious photo-response in the wavelength range of 230–300 nm. Notably, the device based on $Mg_xGa_2O_4$ thin film with $x = 1$ shows the best spectral response characteristics. Its peak responsivity and UV–vis rejection ratio (R_{peak}/R_{400nm}) could reach $\approx0.89\,A\,W^{-1}$ and 10^6, respectively. Moreover, the peak wavelengths and $-3\,dB$ cutoff edges of devices with different Mg contents are slightly different, which may be caused by the substitution of Ga^{3+} (Mg^{2+}) by Mg^{2+} (Ga^{3+}) and the defect states introduced by related processes. In particular, the response

peak can be observed at $\approx250\,nm$ with $-3\,dB$ cutoff edge of $\approx255\,nm$ under 10 V bias for the device based on the film with $x = 1$, which is consistent with the band gap of the $MgGa_2O_4$ film. When the Mg content deviates from the stoichiometric ratio of $MgGa_2O_4$, the responsivity and UV–vis rejection ratio of the devices decreases significantly.

The decay times (t_d) is defined as the time spent when the current drops from 90% to 10% of the maximum value after stopping illumination, and it can be used to characterize the speed of the device. **Figure 5** shows the enlarged view of decay edges of I-t characteristic by 254 nm UV light illumination. It can be seen that devices based on $Mg_xGa_2O_4$ ($x = 0.8$, 1, 1.1) show very fast speed, and their 90–10% t_d are $\approx80\,ms$. When the Mg content deviates greatly from the stoichiometric ratio of $MgGa_2O_4$, the response speed of the device slows down significantly, and 90–10% t_d of $Mg_xGa_2O_4$ devices with $x = 0.6$ and 1.4 are 400 and 480 ms, respectively.

Table 1 summarizes the main performance parameters of $Mg_xGa_2O_4$ films and devices with different Mg contents. Obviously, the $Mg_xGa_2O_4$ SBUV photodetector with $x = 1$ has the highest responsivity, largest UV–vis rejection ratio, and fastest response speed. The optoelectronic performance of the devices gradually deteriorates with the Mg content deviation from the stoichiometric ratio of $MgGa_2O_4$. This phenomenon can be explained by the difference in the crystalline quality of $Mg_xGa_2O_4$ thin films, and higher quality materials have better photodetection properties. In addition, antisite defects, interstitial defects, vacancy defects, and the substitution of Ga^{3+} (Mg^{2+})
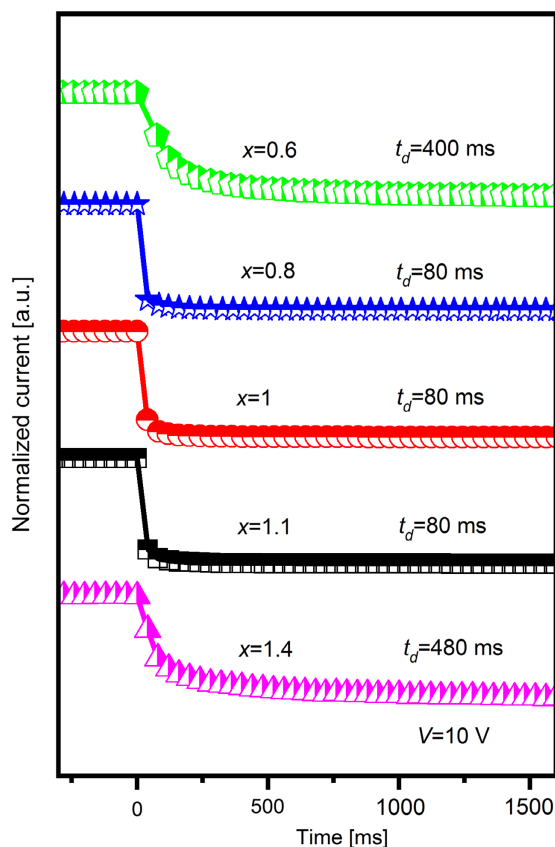
Figure 5. Enlarged view of decay edges of I–t characteristic by 254 nm UV light illumination.

Table 1. Performance parameters of $Mg_xGa_2O_4$ films and devices with different Mg contents.

Mg content [x]	FWHM of Rocking Curve [°]	Responsivity [A W^{-1}]	I_{dark} [pA]	90–10% t_d [ms]	UV-vis rejection ratio
0.6	0.94	9×10^{-4}	12	400	9×10^2
0.8	0.898	0.025	4.7	80	2.5×10^4
1	0.0615	0.89	0.96	80	$\approx 10^6$
1.1	0.104	0.023	0.022	80	2.3×10^4
1.4	0.095	7×10^{-4}	0.82	480	7×10^2

by Mg^{2+} (Ga^{3+}) should also affect the optoelectronic properties of $Mg_xGa_2O_4$, and the detailed mechanism needs to be further clarified.

3. Conclusion

In summary, $Mg_xGa_2O_4$ films with different Mg contents ($x = 0.6$, 0.8, 1, 1.1, and 1.4) were fabricated using MOCVD by regulating the carrier gas flow rate of the Mg source. XRD results show that all samples maintain the spinel structure of $MgGa_2O_4$. And the $Mg_xGa_2O_4$ film with $x = 1$ has the narrowest FWHM of the XRD rocking curve, indicating its high crystalline

quality. In addition, the change of Mg content has little effect on the band gap of $Mg_xGa_2O_4$ films. SBUV photodetectors with MSM structure were constructed on $Mg_xGa_2O_4$ films. Among them, the device based on $Mg_xGa_2O_4$ film with $x = 1$ has the best UV detection performance. At 10 V bias, the dark current is 958 fA, the peak responsivity is 0.89 A W^{-1} at 250 nm, and the UV–vis rejection ratio is as high as 10^6. As the Mg content deviates from the stoichiometric ratio of $MgGa_2O_4$, the photodetection performance of the $Mg_xGa_2O_4$ films shows a significant degeneration, which can be explained by the change in materials crystalline quality. Our findings in this work clarify the effect of Mg content on the properties of $Mg_xGa_2O_4$ thin films and their SBUV photodetectors.

4. Experimental Section

$MgGa_2O_4$ thin films were grown on c-plane sapphire substrates by MOCVD. Before the growth, the substrates were ultrasonically cleaned in trichloroethylene, acetone, absolute ethanol, and deionized water for 5 min, and then dried with high-purity nitrogen. Bis (methylcyclopentadienyl) magnesium ($(MeCp)_2$ Mg), triethylgallium (TEGa), and high-purity oxygen gas were used as precursors for magnesium, gallium, and oxygen, respectively. High-purity nitrogen gas was selected as the carrier gas. The films were grown under a substrate temperature of 650 °C and a pressure of 3000 Pa. The carrier gas flow rates of TEGa and oxygen were kept at 2 and 200 sccm, respectively. To prepare $Mg_xGa_2O_4$ films with different Mg contents, the carrier gas flow rates of $(MeCp)_2$ Mg varied from 5 to 15 sccm. With the increase in Mg source flow rate, more Mg atoms participate in the reaction per unit time, so the growth rate of the film is accelerated. To obtain thin films with similar thickness, the growth time decreased from 120 to 90 min with an increasing Mg source flow rate. After the growth, the $Mg_xGa_2O_4$ films were annealed at 900 °C in an O_2 atmosphere for 15 min. The optical, structural, and surface morphological properties of $Mg_xGa_2O_4$ thin films were characterized by UV-3101 PC scanning spectrophotometer, Bruker D8GADDS X-ray diffractometer and SEM (Hitachi S-4800), respectively. In addition, the elements in the films were qualitatively and quantitatively analyzed by X-ray EDS (EDAX Genesis-2000) operating at 8 KV. To further study the effect of Mg content on the SBUV photodetection performance of $Mg_xGa_2O_4$ thin films, gold interdigitated electrodes were fabricated on the thin films by photolithography and lift-off techniques, thereby realizing the $Mg_xGa_2O_4$ MSM SBUV photodetector. The I–V characteristic curves and I–t curves of the devices were measured with a semiconductor device analyzer (Agilent B1500A).

Supporting Information

Supporting Information is available from the Wiley Online Library or from the author.

Conflict of Interest

The authors declare no conflict of interest.

Data Availability Statement

The data that support the findings of this study are available from the corresponding author upon reasonable request.

Keywords

[1] U. Varshney, N. Aggarwal, G. Gupta, *J. Mater. Chem. C* **2022**, *10*, 1573.

[2] D. Kaur, M. Kumar, *Adv. Opt. Mater.* **2021**, *9*, 2002160.

[3] L. Li, P. S. Lee, C. Y. Yan, T. Y. Zhai, X. S. Fang, M. Y. Liao, Y. Koide, Y. Bando, D. Golberg, *Adv. Mater.* **2010**, *22*, 5145.

[4] L. Tang, B. Tang, H. Zhang, Y. Yuan, *ECS J. Solid State Sci. Technol.* **2020**, *9*, 024009.

[5] D. Li, K. Jiang, X. Sun, C. Guo, *Adv. Opt. Photonics* **2018**, *10*, 43.

[6] Q. Cai, H. F. You, H. Guo, J. Wang, B. Liu, Z. L. Xie, D. J. Chen, H. Lu, Y. D. Zheng, R. Zhang, *Light Sci. Appl.* **2021**, *10*, 94.

[7] X. Liu, K. Mashooq, D. A. Laleyan, E. T. Reid, Z. Mi, *Photonics Res.* **2019**, *7*, B12.

[8] Y. Qin, L. Li, X. Zhao, G. S. Tompa, H. Dong, G. Jian, Q. He, P. Tan, X. Hou, Z. Zhang, S. Yu, H. Sun, G. Xu, X. Miao, K. Xue, S. Long, M. Liu, *ACS Photonics* **2020**, *7*, 812.

[9] Y. Wang, W. Cui, J. Yu, Y. Zhi, H. Li, Z. Y. Hu, X. Sang, E. J. Guo, W. Tang, Z. Wu, *ACS Appl. Mater. Interfaces* **2019**, *11*, 45922.

[10] F. Alema, B. Hertog, P. Mukhopadhyay, Y. Zhang, A. Mauze, A. Osinsky, W. V. Schoenfeld, J. S. Speck, T. Vogt, *APL Mater.* **2019**, *7*, 022527.

[11] G. Kalita, R. D. Mahyavanshi, P. Desai, A. K. Ranade, M. Kondo, T. Dewa, M. Tanemura, *Phys. Status Solidi RRL* **2018**, *12*, 1800198.

[12] X. Chen, K. W. Liu, Z. Z. Zhang, C. R. Wang, B. H. Li, H. F. Zhao, D. X. Zhao, D. Z. Shen, *ACS Appl. Mater. Interfaces* **2016**, *8*, 4185.

[13] S. Vura, U. Muazzam, V. Kumar, S. Vanjari, R. Muralidharan, N. Digbijoy, P. Nukala, S. Raghavan, *ACS Appl. Electron. Mater.* **2022**, *4*, 1619.

[14] M. M. Fan, K. W. Liu, Z. Z. Zhang, B. H. Li, X. Chen, D. X. Zhao, C. X. Shan, D. Z. Shen, *Appl. Phys. Lett.* **2014**, *105*, 011117.

[15] X. Chen, L. Y. Wang, K. W. Liu, Z. Z. Zhang, B. H. Li, J. B. Wu, J. Y. Wang, Y. X. Ni, D. Z. Shen, *J. Mater. Chem. C* **2020**, *8*, 1089.

[16] M. M. Fan, K. W. Liu, X. Chen, X. Wang, Z. Z. Zhang, B. H. Li, D. Z. Shen, *ACS Appl. Mater. Interfaces* **2015**, *7*, 20600.

[17] S. Guo, S. Kang, S. Feng, W. Lu, *J. Phys. Chem. C* **2020**, *124*, 4764.

[18] L. Tien, F. Yang, S. Huang, Z. Fan, R. Chen, *J. Appl. Phys.* **2018**, *124*, 174503.

[19] C. Yan, N. Singh, P. S. Lee, *Appl. Phys. Lett.* **2010**, *96*, 053108.

[20] S. Tsai, S. Basu, C. Huang, L. Hsu, Y. C. Lin, R. Horng, *Sci. Rep.* **2018**, *8*, 14056.

[21] Z. Lou, L. Li, G. Shen, *Nano Res.* **2015**, *8*, 2162.

[22] D. Han, K. Liu, X. Chen, B. Li, T. Zhai, L. Liu, D. Shen, *Appl. Phys. Lett.* **2021**, *118*, 251101.

[23] R. H. Horng, C. Y. Huang, S. L. Ou, T. K. Juang, P. L. Liu, *Cryst. Growth Des.* **2017**, *17*, 6071.

[24] R. H. Horng, P. H. Huang, Y. S. Li, F. G. Tarntair, C. S. Tan, *Appl. Surf. Sci.* **2021**, *555*, 149657.

[25] Q. C. Hou, K. W. Liu, D. Y. Han, Y. X. Zhu, X. Chen, B. H. Li, L. Liu, D. Z. Shen, *Appl. Phys. Lett.* **2022**, *120*, 011101.

[26] Z. Galazka, D. Klimm, K. Irmscher, R. Uecker, M. Pietsch, R. Bertram, M. Naumann, M. Albrecht, A. Kwasniewski, R. Schewski, M. Bickermann, *Phys. Status Solidi A* **2015**, *212*, 1455.

[27] B. Thielert, C. Janowitz, Z. Galazka, M. Mulazzi, *Phys. Rev. B* **2018**, *97*, 235309.

[28] C. Hirschle, J. Schreuer, Z. Galazka, *J. Appl. Phys.* **2018**, *124*, 065111.

[29] A. Kaushal, D. Kaur, *Sol. Energy Mater. Sol. Cells* **2009**, *93*, 193.

[30] B. Lu, X. Cheng, R. Liu, J. Lu, S. Li, L. Chen, Z. Ye, *Appl. Phys. A* **2020**, *126*, 865.

[31] B. P. Uberuaga, M. Tang, C. Jiang, J. A. Valdez, R. Smith, Y. Wang, K. E. Sickafus, *Nat. Commun.* **2015**, *6*, 8750.

[32] E. Korhonen, F. Tuomisto, D. Gogova, G. Wagner, M. Baldini, Z. Galazka, R. Schewski, M. Albrecht, *Appl. Phys. Lett.* **2015**, *106*, 242103.

[33] M. Dong, W. Zheng, C. Xu, R. Lin, D. Zhang, Z. Zhang, F. Huang, *Adv. Opt. Mater.* **2019**, *7*, 1801272.

[34] C. Xu, Z. Du, Y. Huang, M. Dong, R. Lin, Y. Li, B. Wang, W. Zheng, F. Huang, *ACS Appl. Mater. Interfaces* **2018**, *10*, 42681.